Volume 12
Number 23
21 June 2024
Pages 13535–14168

Journal of Materials Chemistry A

Materials for energy and sustainability

rsc.li/materials-a

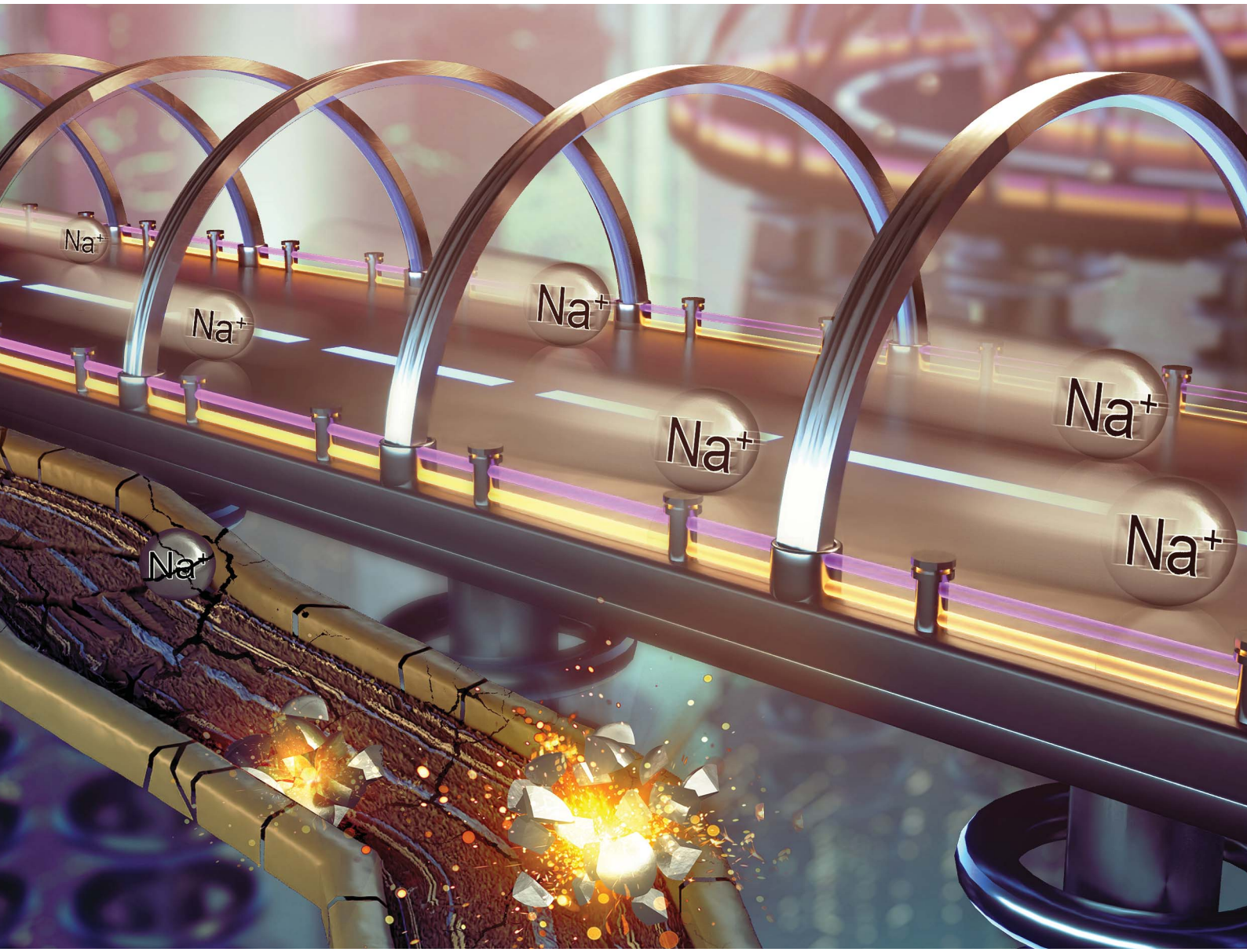

ISSN 2050-7488

ROYAL SOCIETY OF CHEMISTRY

PAPER

Ming-Sheng Wang *et al.*

Pore-size tuning of hard carbon to optimize its wettability for efficient Na^+ storage

Journal of Materials Chemistry A

ROYAL SOCIETY OF CHEMISTRY

PAPER

View Article Online
View Journal | View Issue

Cite this: J. Mater. Chem. A, 2024, 12, 13703

Pore-size tuning of hard carbon to optimize its wettability for efficient Na^+ storage†

Lin Guo,[a] Minyi Huang,[a] Weicheng Liu,[ab] Hanqi Zhu,[a] Yong Cheng[a] and Ming-Sheng Wang *[ac]

Received 4th April 2024
Accepted 19th May 2024

DOI: 10.1039/d4ta02303j

rsc.li/materials-a

Hard carbons hold great promise as the anode materials for sodium-ion batteries (SIBs), but the limited capacities and sluggish Na^+ transfer kinetics still hinder their practical applications. These issues can be addressed from the perspective of improving the wettability of hard carbons with electrolyte. Herein, we demonstrate that the wettability of hard carbons can be regulated by tuning their pore size, so as to optimize their electrochemical properties. A series of N-doped hollow mesoporous carbon nanotubes (HMCNTs) with the average pore sizes in the range of 2–8 nm are synthesized. Among them, the HMCNTs with an average pore size of 6.1 nm (HMCNTs-6.1) exhibits the most improved wettability and reaction kinetics, which delivers a high reversible capacity (415.5 mA h g^{-1} after 100 cycles at 0.1 A g^{-1}), superior long-term cycle stability and rate capability. In addition, as visualized by *in situ* transmission electron microscopy, the HMCNTs-6.1 with relatively large mesopores is more favorable for the mass transport across the carbon shells than the HMCNTs with smaller pore sizes. This work provides new insight for understanding the relationship between pore size, electrolyte wettability and electrochemical performance of porous hard carbon, which can help to design the high-performance SIB anodes.

1. Introduction

The past decade has witnessed an increasing demand for more sustainable and affordable electrochemical energy storage (EES) solutions beyond Li-ion batteries (LIBs).[1–3] On account of the high abundance and low cost of Na metal, rechargeable sodium-ion batteries (SIBs) are considered to be an ideal alternative to LIBs in specific fields, such as large-scale energy storage systems and short-distance transportation vehicles.[4,5] However, due to the larger ionic radius of Na^+ (0.102 nm) than Li^+, the insertion/de-insertion processes of Na^+ leads to the large volume expansion, lower energy density and decreased cyclic stability of the graphite anodes used in SIBs.[6,7] Compared to graphite, hard carbon with a large number of defects and adjustable interlayer spacing has been demonstrated to be a promising anode material for SIBs.[8,9] Moreover, other merits of hard carbon, such as the chemical inertness, good electrical conductivity, abundant resource and low cost, *etc.*, endow it with great potential for commercial use.[10,11] Hard carbon with porous structure demonstrates exceptional Na^+ storage performance, high capacity, and enduring stability.[12,13] However, hard carbon still suffers from the insufficient transport and reaction kinetics, the relatively low capacity, as well as the low initial coulomb efficiency (ICE), *etc.*[14,15]

In order to solve these problems, various pore structures are widely introduced to the architecture design of hard carbon, which can not only effectively buffer the volume change during cycling, but also provide large available specific surface areas to enlarge electrode/electrolyte interface and shorten the diffusion path of ions.[16–19] To further improve the ionic conductivity and the specific capacity of carbonaceous material in SIBs, heteroatom (N, O, S and P, *etc.*) doping is also commonly employed, which is capable of altering the surface chemistry and thereby the electrochemical properties of the materials.[20,21] Another approach to promote the kinetics of carbonaceous anodes is to enhance their wettability with electrolytes. Several recent studies have confirmed the effect of enhanced wettability on the improvement of anode performance, which is usually achieved by chemical modification.[22,23] However, so far, there have been relatively few attempts to improve the wettability from the perspective of pore engineering, and especially the pore-size effect on the wettability and anode performance of hard carbons remains unclear.

Herein, a series of N-doped hollow mesoporous carbon nanotubes (HMCNTs) with tunable pore size were synthesized for use as SIB anodes. The wettability of these HMCNTs, as

[a]State Key Lab of Physical Chemistry of Solid Surfaces, College of Materials, Xiamen University, Xiamen 361005, China. E-mail: mswang@xmu.edu.cn

[b]Key Laboratory of Advanced Metallic Materials of Jiangsu Province, School of Materials Science and Engineering, Southeast University, Nanjing, 211189, People's Republic of China

[c]Fujian Key Laboratory of Surface and Interface Engineering for High Performance Materials (Xiamen University), Xiamen Key Laboratory of High Performance Metals and Materials (Xiamen University), China

† Electronic supplementary information (ESI) available. See DOI: https://doi.org/10.1039/d4ta02303j

a function of pore size, was systematically compared and linked with their Na^+ storage performance. The wettability can be significantly enhanced by these through-holes, which can draw the electrolyte into inner cavities efficiently by capillarity. Consequently, a satisfactory electrolyte/anode contact was established, effectively reducing ion diffusion paths, achieving uniform distribution of ion flux. Specifically, the HMCNTs with an average pore size of 6.1 nm (HMCNTs-6.1) exhibited the most improved wettability and electrochemical performance, which had a high reversible capacity (415.5 mA h g^{-1} after 100 cycles at 0.1 A g^{-1}), superior long-term cycle stability and rate capability. In addition, *in situ* transmission electron microscopy (TEM) was conducted to confirm that HMCNTs-6.1 exhibited a pronounced effect of capillarity. This work provides valuable insight for improving the electrolyte wettability and Na^+ transport kinetics of hard carbon from the perspective of pore-size tuning, which can be helpful for the design of advanced anodes for SIBs.

2. Results and discussion

The hollow mesoporous carbon nanotubes were synthesized using a template method, as illustrated in Fig. 1. Tetrapropoxysilane (TPOS) was selected as the source of SiO_2, and MnO_2 nanowires were employed as the sacrificial template. Initially, SiO_2 was coated onto MnO_2 nanowires to obtain MnO_2@SiO_2 through the hydrolysis of TPOS in the solution. Then, the resorcinol-formaldehyde resin (produced by the polymerization of resorcinol and formaldehyde) and silicon dioxide (by hydrolysis of remaining TPOS) were co-condensed onto the MnO_2@SiO_2 nanowires, forming a coating layer mixed with resin and SiO_2 on the nanowire surface (MnO_2@SiO_2@-resin&SiO_2). After the carbonization and the removal of SiO_2 by HF, the hollow carbon nanotubes with open mesochannels in the tube walls were obtained (Fig. 1). Ammonia was used as both a pH regulator and catalyst during the synthesis, leading to a uniform distribution of nitrogen atoms in the synthesized hollow mesoporous carbon nanotubes, *i.e.* forming N-doped HMCNTs. To further adjust the size of mesopores, a pore engineering technique was used to control the pore size of the N-doped HMCNTs. By adding TEOS with various mass ratios during polymerization, N-doped HMCNTs with smaller pore sizes were prepared. Conversely, to increase the pore size, we can modify the water-to-ethanol ratio during the polymerization process (Fig. 1b). The mechanism behind the pore size tuning of hard carbon is discussed in ESI.†

Fig. 2 shows five types of as-synthesized N-doped HMCNTs with average pore sizes of 2.3 nm, 4.2 nm, 5.1 nm, 6.1 nm and 7.7 nm, respectively, which are denoted as HMCNTs-2.3 (Fig. 2a), HMCNTs-4.2 (Fig. 2b), HMCNTs-5.1 (Fig. 2c), HMCNTs-6.1 (Fig. 2d) and HMCNTs-7.7 (Fig. 2e). As shown in the scanning electron microscopy (SEM) and transmission electron microscopy (TEM) images, all these HMCNTs exhibited similar hollow tubular morphologies, with the mesochannels vertically oriented with respect to the wall surface. As the pore size increased, the nanotube surface became rougher and the pore structures were more easily discernible. In addition, we attempted to further increase the average pore size to more than 7.7 nm by adjusting the synthesis conditions, but failed. The resultant nanotubes had an average pore size of only 7.6 nm (HMCNTs-7.6), and the shells were significantly fragmented, even leading to a broken tube structure (Fig. S1†). Such nanotubes also demonstrated inferior performance in Na^+ storage. Therefore, the data of HMCNTs-7.6 are not listed here for comparison. The characterization and electrochemical test results of HMCNTs-7.6 are presented in ESI (Fig. S8 and S9).†

EDS mapping of the samples (Fig. S2†) reveals the uniform distribution of N and O elements in the carbon shells. The X-ray diffraction (XRD) patterns (Fig. S4a†) of the five samples present a broad diffraction peak at around 24°, indexed to (0 0 2) planes, which is typical of amorphous hard carbon.[24] The Raman spectra (Fig. S4b†) display two dominant peaks centered at 1345 (D band) and 1592 cm^{-1} (G band).[25] As expected, the five types of HMCNTs show the similar intensity ratio of I_D/I_G (~1.00), suggesting comparable defective degrees.[26] In addition, X-ray

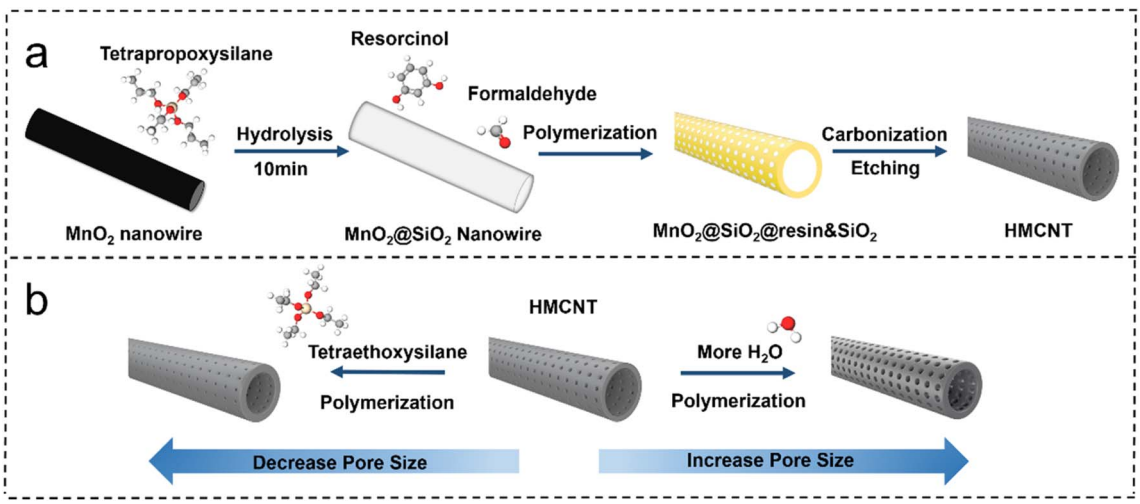

Fig. 1 (a) Schematic diagram of the synthesis route of HMCNTs. (b) Pore-size tuning of HMCNTs.

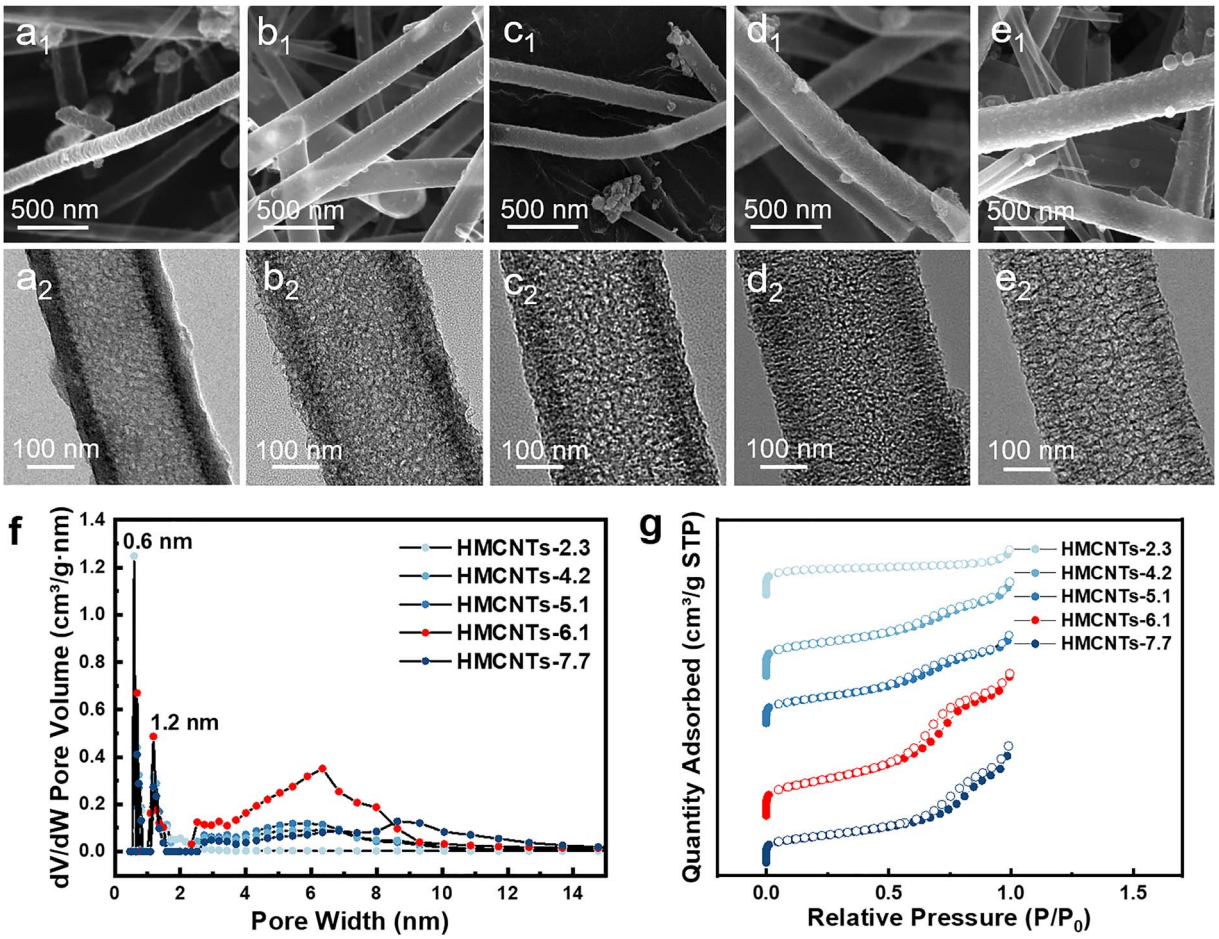

Fig. 2 SEM and TEM images of (a) HMCNTs-2.3; (b) HMCNTs-4.2; (c) HMCNTs-5.1; (d) HMCNTs-6.1; (e) HMCNTs-7.7; (f) pore size distributions of these HMCNTs and (g) the corresponding N_2 isothermal adsorption/desorption curves.

photoelectric spectroscopy (XPS) indicates the presence of carbon, nitrogen, and oxygen in the HMCNTs. The high-resolution C 1s XPS spectra of five samples (Fig. S5 and S6†) all comprise C–C, C–O, and C=O bonds, and all the N 1s XPS spectra can be deconvoluted into the peaks of pyridinic N and pyrrolic N, which suggest similar chemical properties of the five HMNCTs.[27–29]

To further reveal the difference and quantify the pore size of the series of carbon nanotubes, we conducted BET tests on all the samples. Obviously, there is a prominent increase of the slope in adsorption/desorption curve at P/P_0 = 0.6–0.8 in the isothermal plots (Fig. 2g) of HMCNTs-6.1, which is more significant than the other HMCNTs. This can be attributed to the capillary condensation of N_2 in the mesochannels. According to the pore size distribution (Fig. 2f), large numbers of micropores with sizes peaked at about 0.6 and 1.2 nm can be confirmed in all five samples. Different from the HMCNTs-2.3, HMCNTs-4.2 and HMCNTs-5.1 with the smaller pore size, the HMCNTs-6.1 possessed remarkable mesoporous features, as evidenced by the broad peaks at 6 nm. We observed that increasing the mesopore diameter appropriately can enlarge both the specific surface area and pore volume of HMCNTs. The increase of surface area suggests more active sites for Na-ion insertion/extraction, and the enlargement of pore volume can accommodate volume change of material during cycling and ensure sufficient electrolyte infiltration into the electrode.

To experimentally verify whether the capillarity of mesochannels can promote the wettability between these nanotube electrodes and electrolyte at macro scale, the electrolyte (1 M $NaPF_6$ in DME) was dripped onto the electrodes (made of the five types of HMCNTs, respectively) to measure the dynamic contact angles. As shown in Fig. 3a–e, the contact angle between the electrolyte and HMCNTs-6.1 quickly approached zero, while the other four samples exhibited appreciable contact angles at 0.6 s, suggesting superior electrolyte wettability of HMCNTs-6.1 over the other nanotubes. Besides, the contact angle (see *e.g.* those at 0.6 s in Fig. 3f) decreased monotonically as the average pore size increased up to 6.1 nm, but increased if the pore size was enlarged to 7.7 nm, suggesting that increasing the pore size of HMCNTs does not always improve their wettability with electrolyte. To elucidate the connection between pore size and wettability, we further examined the BET data of these nanotubes. As shown in Fig. 3g, both specific surface area and pore volume peaked at pore size of 6.1 nm. This indicates that appropriate pore enlargement can maximize the specific surface area and pore volume of carbon nanotubes, which is

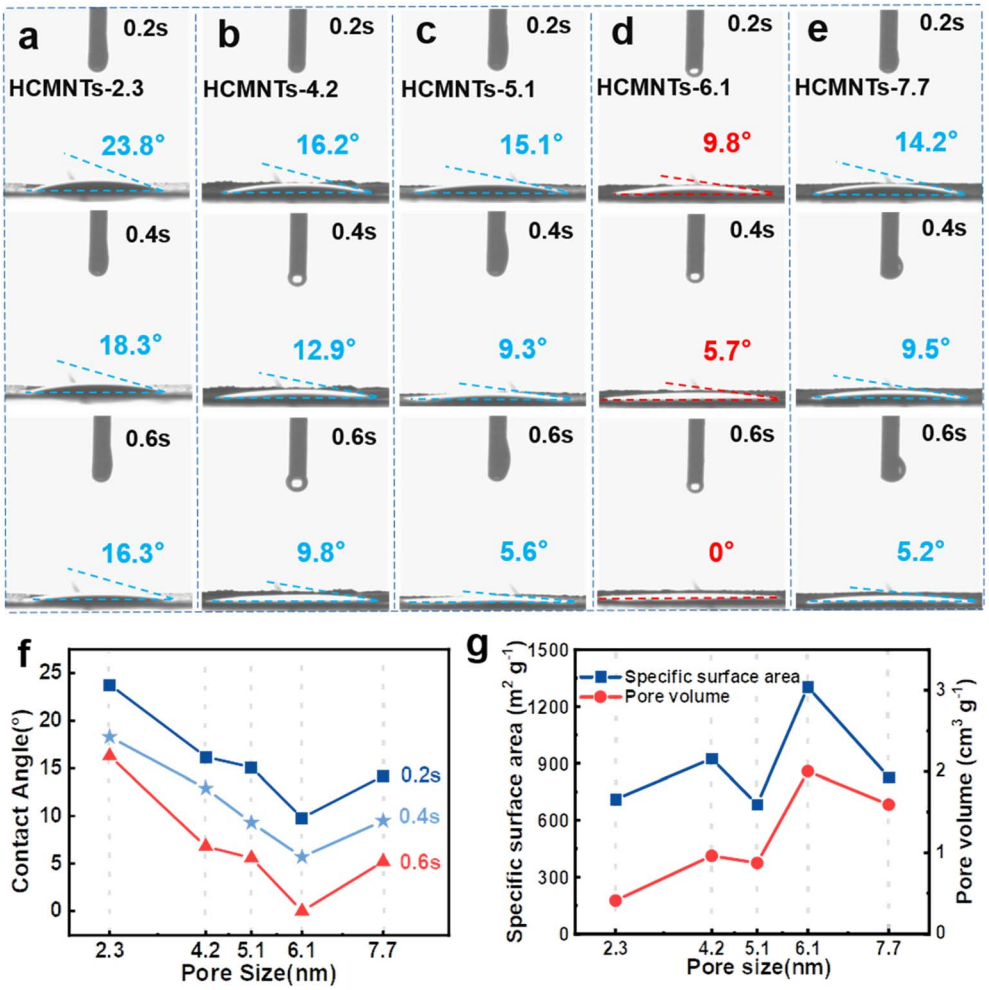

Fig. 3 (a–e) Dynamic contact angles between the electrolyte and HMNCTs series electrodes with pore sizes of 2.3, 4.2, 5.1, 6.1 and 7.7 nm, respectively; (f) contact angle-pore size curves at different time; (g) specific surface area and pore volume of HMNCTs at different pore sizes.

critical for enhancing the wettability between the electrode and electrolyte. Note that despite the larger pore size of HMCNTs-7.7, its surface area and pore volume were reduced compared to HMCNTs-6.1. It might be possible that excessive enlargement of the pore size can significantly reduce the number of pores, and therefore the specific surface area and pore volume. In short, HMCNTs-6.1 exhibited the optimized pore size effect in terms of electrolyte wettability.

In order to investigate the mechanism and kinetics of the electrode reaction, half coin cells were assembled to perform the electrochemical tests. To explore the electrochemical kinetics of Na^+ storage in the five electrodes, cyclic voltammetry (CV) rate tests were conducted at different scan rates ranging from 0.2 to 1.0 mV s^{-1} (Fig. 4a and S7†). Fig. 4a shows the CV curves of HMCNTs-6.1 at different scan rates, and the curves maintain a consistent shape from 0.2 mV s^{-1} to 1.0 mV s^{-1}, owing to the good mechanical and electrochemical stability of HMCNTs-6.1. Fig. 4b displays the initial 3 cycles of cyclic voltammetry (CV) curves of HMCNTs-6.1 in a voltage window of 0.01–3.0 V (*vs.* Na/Na^+) at the scan rate of 0.2 mV s^{-1}. A sharp cathodic peak appears at 1.0 V in the first cycle and disappears in the following cycles, which can be mainly attributed to the decomposition of electrolyte and the formation of SEI.[1,30] The redox peak at near 0.02 V/0.25 V refer to the intercalation/deintercalation of Na^+ into graphitic domain.[31] Furthermore, we can evaluate the pseudocapacitive contribution ratio of these electrodes by eqn (1):

$$i = k_1\nu + k_2\nu^{1/2} \quad (1)$$

in which $k_1\nu$ and $k_2\nu^{1/2}$ represent the capacity contribution from pseudocapacitive and diffusion-controlled processes, respectively.[32–34] In Fig. 4c and S7,† HMCNTs-6.1 shows the highest pseudocapacitive contribution ratios of all samples. This suggests that the strategy of pore size regulation can substantially increase the electrode/electrolyte interface area, thus facilitating the pseudocapacitive behavior of Na^+ in hard carbon, which can effectively promote the rate performance of the anode,[35,36] as also evidenced in Fig. 5c.

As mentioned above, the greatly enhanced wettability of the mesoporous carbons can be attributed to the strong capillarity of the open mesochannels in carbon tube walls, which can draw

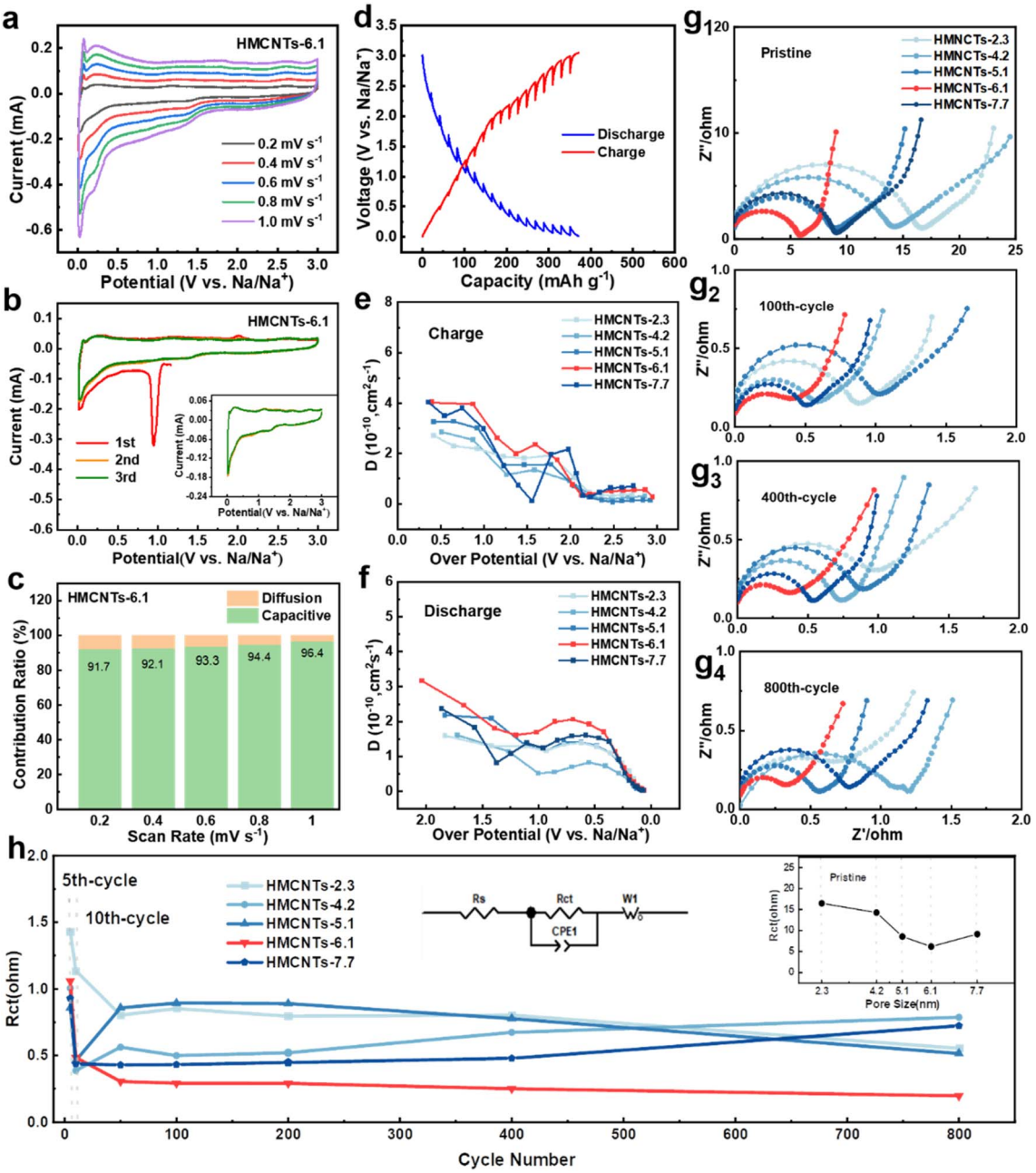

Fig. 4 (a) CV curves at different current densities of HMCNTs-6.1. (b) CV curves at 0.2 mV s^{-1} of HMCNTs-6.1. (c) Pseudocapacitive contribution ratios of HMCNTs-6.1 at different current densities. (d) GITT potential profile of HMCNTs-6.1. (e) D_{Na^+} of HMCNTs series in the charge process. (f) D_{Na^+} of HMCNTs series in the discharge process. (g) Nyquist fitting plots of the five HMCNTs at different cycles and (h) the comparison of their R_{ct} values after fitting.

the electrolyte into the cavity and then sufficiently infiltrate the electrode, so that the huge specific surface area can be fully utilized. This assumption is supported by the results of diffusion coefficient tests. As shown in Fig. 4d, galvanostatic intermittent titration technique (GITT) was carried out to measure the diffusion coefficient of the electrodes. The numerical value of diffusion coefficient D_{Na^+} can be evaluated by eqn (2):

$$D_{Na^+} = \frac{4}{\pi\tau}\left(\frac{m_b V_M}{M_B A}\right)^2\left(\frac{\Delta E_s}{\Delta E_\tau}\right) \quad (2)$$

where M_B and V_M refer to the molar mass and volume, m_b and A refer to the mass and area of the active materials loaded on the electrode.[37,38] According to the results (Fig. 4e and f), the overall diffusion coefficients of the HMCNTs-6.1 are significantly larger than the other four samples in both charge and discharge processes. Since the five types of HMCNTs were similar in chemistry, and also shared the similar defective features (*i.e.* the approximately same I_D/I_G ratios in Fig. S4b†), their different diffusion coefficient should be mainly ascribed to the difference in porous architecture. Among the five HMCNTs, the pore

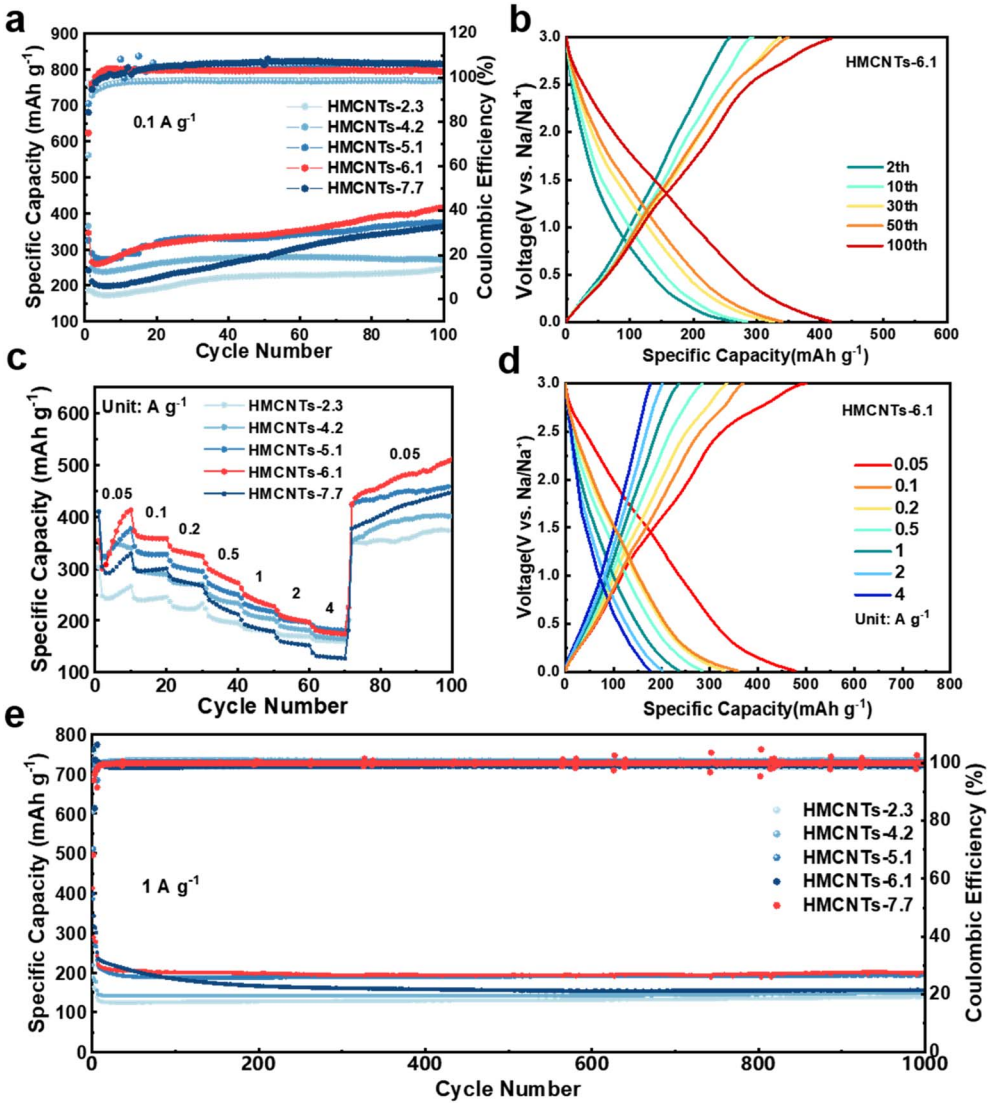

Fig. 5 (a) Cycling performance at 0.1 A g^{-1} of the series of HMCNTs. (b) Charge/discharge curves at 0.1 A g^{-1} of HMCNTs-6.1. (c) Rate performance of the five HMCNTs. (d) Charge/discharge curves at different current densities of HMCNTs-6.1. (e) Cycling performance at 1 A g^{-1} of the five HMCNTs.

structure of HMCNTs-6.1 is the most favorable for promoting the electrolyte wettability and the ion transport efficiency, thus resulting in higher diffusion coefficient.[39]

Fig. 4g shows the electrochemical impedance spectroscopy measurements of five types of HMCNTs at different cycles. The charge-transfer resistance (R_{ct}) value of the HMCNTs-6.1 electrode gradually decreases from 6.17 Ω to 0.48 Ω after 10 cycles and then becomes stable, which can be attributed to the structure reconstruction and conductivity improvement caused by the Na^+ insertion.[40,41] As shown in Fig. 4h, HMCNTs-6.1 possesses the minimum R_{ct} values among the five hard carbons during the whole processes, which suggests the excellent long-term electrolyte wettability of HMCNTs-6.1 and the fastest Na^+ reaction kinetics. Notably, as shown in the inset of Fig. 4h, the R_{ct} of the five pristine HMCNTs exhibits the same dependence on pore size with the contact angle (Fig. 3f), indicating the strong linkage between the reaction kinetics and electrolyte wettability of the samples.

As shown in Fig. 5a, when cycled at 0.1 A g^{-1}, HMCNTs-6.1 delivered a discharge capacity of 345.3 mA h g^{-1} with an initial coulombic efficiency (ICE) of 75.0% in the first cycle. From the second cycle, the specific capacity of the cell became stable and the coulombic efficiency (CE) increased gradually. At the 100th cycle, the cell can still deliver a specific capacity of 415.5 mA h g^{-1} with a CE of nearly 100%. In comparison, the HMCNTs-2.3, HMCNTs-4.2, HMCNTs-5.1 and HMCNTs-7.7 cells delivered specific capacities of 247.4 mA h g^{-1}, 270.4 mA h g^{-1}, 375.3 mA h g^{-1}, and 363.5 mA h g^{-1} at 0.1 A g^{-1} after 100 cycles, respectively. Generally, as the pore size of the HMCNTs increases, the cell gains a higher specific capacity. HMCNTs-6.1 exhibited much higher capacity than the other four types of HMCNTs due to the enhanced wettability as

discussed above. Samples with larger pores demonstrate more pronounced capillary action compared to those with smaller pores and thus have higher electrolyte wettability. Furthermore, during the cycling process, HMCNTs-5.1, HMCNTs-6.1, and HMCNTs-7.7 all exhibited an increasing trend of capacity, which can be attributed to the continuous electrolyte penetration in the mesoporous carbon electrodes throughout the cycling. For these three types of carbon nanotubes, the effective contact area gradually increases, leading to continuous increase in capacity. Conversely, for carbon nanotubes with smaller pore sizes such as HMCNTs-2.3 and HMCNTs-4.2, electrolyte penetration is limited, resulting in a less variation in the contact area between the electrolyte and electrode materials over time. Fig. 5b shows the typical charge/discharge curves of HMCNTs-6.1.

Meanwhile, compared to the other four types of HMCNTs, HMCNTs-6.1 exhibited superior rate performance, delivering capacities of 358.5, 331.3, 284.9, 236.4 and 201.8 mA h g^{-1} at 0.1, 0.2, 0.5, 1 and 2 A g^{-1}, respectively (Fig. 5c). Even at a high current density of 4 A g^{-1}, it still retained a specific capacity of 176.6 mA h g^{-1}. Moreover, when the current density switched back to 0.05 A g^{-1} after cycling at 4 A g^{-1}, the specific capacity of HMCNTs-6.1 can reach as high as 450 mA h g^{-1}. This confirms that adjusting the pore size of hard carbon to enhance its wettability with the electrolyte can lead to faster kinetics. As shown in Fig. S10,† the rate performance of our samples was quite competitive compared with the recently reported carbonaceous SIB anodes with excellent rate performances.

Then, we further tested the long-term cyclability of HMCNTs at high current density (Fig. 5e). The coin cell was first cycled at 0.1 A g^{-1} for 3 times to compensate the capacity loss, and then at a current density of 1 A g^{-1} to test the long-term cyclability. HMCNTs-6.1 delivered a high specific capacity of 278.08 mA h g^{-1} after the pre-sodiation, and the capacity was maintained at around 200 mA h g^{-1} in subsequent cycles, outperforming the cycling specific capacities of HMCNTs-2.3, HMCNTs-4.2, HMCNTs-5.1, and HMCNTs-7.7. This further demonstrates that the Na^+ storage capability of hard carbon can be markedly enhanced by appropriate pore size tuning.

To visualize and compare the pore size effect on the shell sodiation and Na ion transport behavior of the HMCNTs, *in situ* TEM experiments were conducted. Two typical HMCNT with small (2.3 nm) and large (6.1 nm) pore sizes were selected for comparison. Fig. 6a illustrates the experimental setup, where a single HMCNT located on the Mo tip servers as the working electrode, while a Na/Na_2O metal located on the Cu tip works as both the solid electrolyte and the counter electrode. Once the contact between a nanotube and the counter Na/Na_2O electrode was established, a bias of −3 V was applied to the nanotube to initiate the reaction. Fig. 6b and c exhibits the time-resolved TEM images of HMCNT-2.3 and HMCNT-6.1 during sodiation, respectively. For HMCNT-2.3 (Fig. 6b), after 296.0 s of sodiation, the outer diameter expanded from 186.4 nm to 194.0 nm by 4.1%, while the cavity of the nanotube remained empty. For HMCNT-6.1 as shown in Fig. 6c, the nanotube experienced a slight expansion of only 1.2%, demonstrating its structural advantage of the large pores to butter the volume expansion during sodiation. Interestingly, Na metal nucleated at the bottom of the nanotube and grew upward during further reaction. As revealed by the selected-area electron diffraction (SAED)

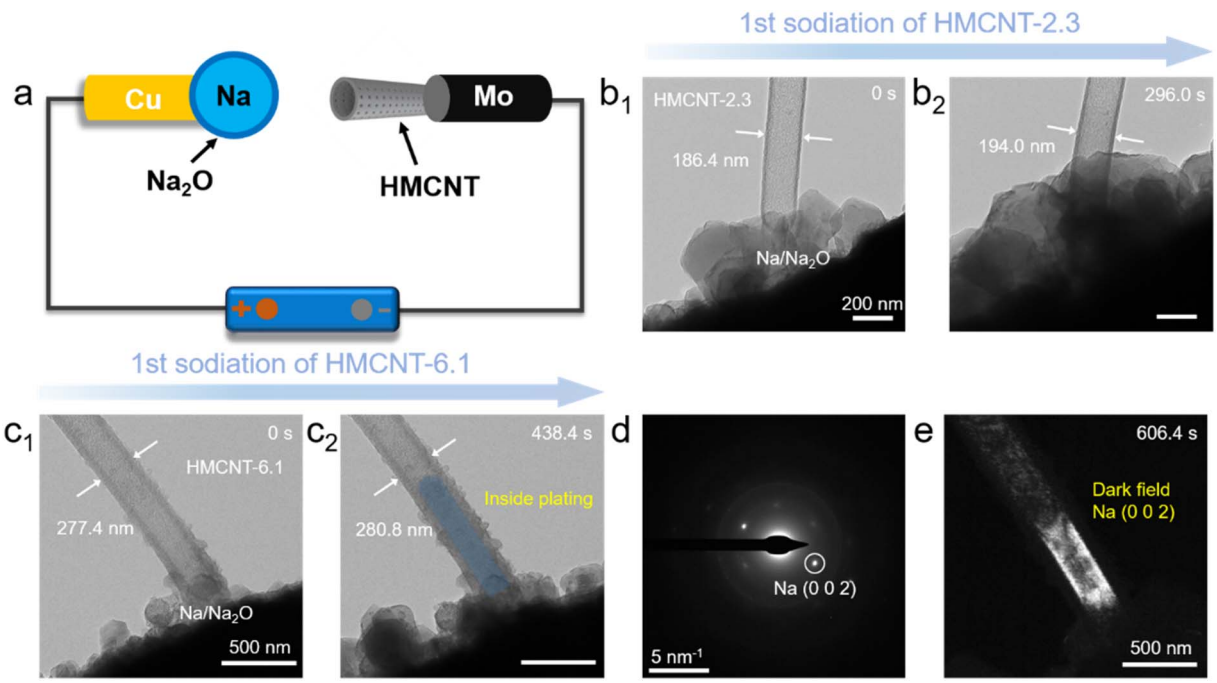

Fig. 6 (a) Schematic illustration of the *in situ* TEM nanobattery configuration. *In situ* TEM images of sodiation and plating processes for (b) HMCNT-2.3 and (c) HMCNT-6.1 (d) SAED pattern of the Na-filled HMCNT-6.1 (e) dark-field image of the HMCNT-6.1 formed by selecting the diffraction spot of Na (002).

pattern from the Na-filled HMCNT-6.1 (Fig. 6d), the sharp spots are indexed as metallic Na, indicating its single-crystalline nature. The dark field (DF) image formed by selecting the sharp diffraction spot of Na (002) demonstrates that the single-crystal Na occupied the entire inner spaces of HMCNT-6.1 (Fig. 6e). The Na deposition inside HMCNT-6.1 indicates that Na ions can easily penetrate the carbon shell through the larger mesochannels. In contrast, the small pores in HMCNT-2.3 may be blocked during the sodiation process, which slows down the inward diffusion of Na ions. The driving force for Na encapsulation is the drop in Gibbs free energy associated with the Na nucleation inside a nanotube compared to its outside nucleation,[42] similar to the capillary force that drive the liquid electrolyte into the HMCNTs. Our *in situ* TEM experiments, though conducted in a solid-state environment, suggests that the sub-10 nm mesopores with larger size are more favorable for the mass transport and electrolyte infiltration, thus greatly promoting the wettability of HMCNT-6.1.

3. Conclusion

In summary, we proposed a pore size tuning strategy to regulate the electrolyte wettability of carbonaceous anodes for improving Na^+ transport kinetics. The effects of pore size on the promoted electrolyte wettability and reaction kinetics of hard carbon were thoroughly evaluated by various characterizations. It is demonstrated that increasing the pore size appropriately can enhance the specific surface area and pore volume of carbon nanotubes, thereby improving the electrode's wettability to electrolyte and its reaction kinetics. The HMCNTs-6.1 electrode demonstrate the optimal electrochemical performance among the series of HMCNTs anodes. This work provides new insight for enhanced Na^+ storage from the perspective of the pore-size tuning of mesoporous hard carbons, which can be practically used in the design of advanced SIB anodes.

4. Experimental section

Preparation of HMCNTs

First, 2 mmol $MnSO_4 \cdot H_2O$, 3.5 mmol $KClO_3$ and 3.5 mmol CH_3COOK were dissolved in 30 mL deionized water with stirring to form a clear solution. After adding 1.6 mL acetic acid, the solution was transferred to a 50 mL Teflon-lined autoclave and then kept in an oven at 160 °C for 8 hours. The resulting product collected by centrifugation was MnO_2 nanowires. Then, these MnO_2 nanowires as the template were added into a solution that contained 10 mL deionized water, 3 mL 30 wt% ammonia and 70 mL ethanol. After thorough stirring, 2 mL tetrapropoxysilane (TPOS) was added in this solution with stirring at 30 °C for 10 minutes. Then, 400 mg resorcinol and 0.56 mL 37 wt% formaldehyde were added into the solution under stirring for 24 hours. The precursor of HMCNT6.1 was obtained by centrifugation, washed by deionized water and ethanol, and dried at 60 °C for 8 hours. After carbonized at 800 °C at a heating rate of 2 °C per minute under Ar atmosphere for 4 hours, we can obtain SiO_2@HMCNTs-6.1. To remove SiO_2, the resulting product was washed by 15 wt% hydrofluoric acid. The final product of HMCNTs-6.1 was thus obtained.

The preparation process of HMCNTs-2.3, HMCNTs-4.2 and HMCNTs-5.1 was similar with that of HMCNT6.1, and the only difference was that the 2 mL TPOS in the above preparation scheme is replaced by an equal amount of TPOS/tetraethoxysilane (TEOS) mixture (with volume ratios of 0 : 1, 1 : 2, 2 : 1, respectively). The preparation process of HMCNT7.6 and HMCNTs-7.7 was also similar with that of HMCNT6.1, and the only difference was to change the ethanol/water ratio in the above preparation scheme (5 : 3, 6 : 2, respectively).

Material characterization

Scanning electron microscopy (SEM, Zeiss SIGMA) and Transmission electron microscopy (TEM, FEI Talos F200s) were utilized to characterize the morphology and microstructure of the samples. Specific surface areas and pore sizes distribution were measured by N_2 isothermal adsorption and desorption with Micromeritics ASAP 2460 analyzer. Photos of the contact angle between electrolyte (1 M $NaPF_6$ in DME) and electrode were taken with the use of KrüSS DSA100 drop shape analyzer. X-ray Diffraction (XRD) analysis was performed on a Bruker-AXS D8-A25 X-ray diffractometer equipped with Cu-K_α radiation. Raman spectra were conducted on Horiba France Sas HR Evolution confocal Raman microscope using a 532 nm excitation laser. X-ray photoelectron spectroscopy (XPS) was conducted on a Thermo Scientific K-Alpha spectrometer equipped with Al Kα radiation.

Electrochemical measurements

The samples, *i.e.* the active materials, were mixed with conductive agent (Super P) and carboxymethylcellulose binder with a weight ratio of 75 : 10 : 15 to form homogeneous slurry. The slurry was pasted on Cu foil uniformly and dried under vacuum at 60 °C overnight. The mass loading of the active material was weighed to be 0.8–1.0 mg cm^{-2}. The coin cells (2016) were assembled in an Ar-filled glove box (Mikrouna), in which the concentration of H_2O and O_2 were maintained below 1 ppm. The Cu foil pasted with active material was used as working electrode, sodium metal was used as counter/reference electrode, glass fiber was used as separator, and the electrolyte was a 1 M $NaPF_6$ solution dissolved in dimethyl ether (DME).

The long-term cycling measurements and rate capability tests were conducted at 30 °C by Neware MIHW-200-160CH integrated constant temperature cells testing system. GITT measurements were performed by LAND-CT2001A at room temperature within a potential range of 0.01–3.0 V (*vs.* Na/Na^+). CV and EIS curves were collected on Chenhua CHI660E electrochemical workstation.

In situ TEM observations

The sodiation/plating behaviors of our materials were *in situ* observed in FEI Talos F200s TEM with 200 kV acceleration voltage. The HMCNTs samples were attached to a molybdenum tip that acted as the working electrode, a small amount of Na metal was loaded on a Cu tip that worked as the counter

electrode, and the naturally formed Na_2O wrapped on Na metal served as the solid electrolyte. Thus, we constructed a nanoscale cell to mimic the circumstance for sodium ion insertion into our materials. A constant bias of −3.0 V was applied to the working electrode when the Na_2O/Na electrode was brought into contact with our materials to trigger the sodiation/plating processes.

Conflicts of interest

There are no conflicts to declare.

Acknowledgements

This work was financially supported by the National Natural Science Foundation of China (Grants No. 52172240), the China Postdoctoral Science Foundation (Grants No. 2022M712655), the Fundamental Research Funds for the Central Universities (Grant No. 20720230043), and the "Double-First Class" Foundation of Materials and Intelligent Manufacturing Discipline of Xiamen University.

References

1 X. Y. Chen, J. Y. Tian, P. Li, Y. L. Fang, Y. J. Fang, X. M. Liang, J. W. Feng, J. Dong, X. P. Ai, H. X. Yang and Y. L. Cao, *Adv. Energy Mater.*, 2022, **12**, 2200886.
2 Y. S. Tian, G. B. Zeng, A. Rutt, T. Shi, H. Kim, J. Y. Wang, J. Koettgen, Y. Z. Sun, B. Ouyang, T. N. Chen, Z. Y. Lun, Z. Q. Rong, K. Persson and G. Ceder, *Chem. Rev.*, 2021, **121**, 1623–1669.
3 J. X. Xu, Y. W. Liu, C. W. Xu, J. Li, Z. W. Yang, H. H. Yan, H. X. Yu, L. Yan, L. Y. Zhang and J. Shu, *Coord. Chem. Rev.*, 2023, **474**, 214867.
4 F. Xie, Z. Xu, Z. Y. Guo, Y. X. Lu, L. Q. Chen, M. M. Titirici and Y. S. Hu, *Sci. China Chem.*, 2021, **64**, 1679–1692.
5 H. M. Zhang, S. W. Zhao and F. Q. Huang, *J. Mater. Chem. A*, 2021, **9**, 27140–27169.
6 C. Bommier, T. W. Surta, M. Dolgos and X. L. Ji, *Nano Lett.*, 2015, **15**, 5888–5892.
7 R. A. Adams, A. Varma and V. G. Pol, *Adv. Energy Mater.*, 2019, **9**, 1900550.
8 S. Qiu, L. F. Xiao, M. L. Sushko, K. S. Han, Y. Y. Shao, M. Y. Yan, X. M. Liang, L. Q. Mai, J. W. Feng, Y. L. Cao, X. P. Ai, H. X. Yang and J. Liu, *Adv. Energy Mater.*, 2017, **7**, 1700403.
9 X. W. Dou, I. Hasa, D. Saurel, C. Vaalma, L. M. Wu, D. Buchholz, D. Bresser, S. Komaba and S. Passerini, *Mater. Today*, 2019, **23**, 87–104.
10 A. Ponrouch, A. R. Goñi and M. R. Palacín, *Electrochem. Commun.*, 2013, **27**, 85–88.
11 D. Q. Chen, W. Zhang, K. Y. Luo, Y. Song, Y. J. Zhong, Y. X. Liu, G. K. Wang, B. H. Zhong, Z. G. Wu and X. D. Guo, *Energy Environ. Sci.*, 2021, **14**, 2244–2262.
12 C. C. Sun, F. J. Kong, L. L. Fan, S. Tao, G. K. Zhang, S. Q. Chu, W. S. Chu and L. Song, *Chem. Eng. J.*, 2023, **470**, 144419.
13 X. C. Sun, X. Gao, Z. Li, X. Zhang, X. L. Zhai, Q. X. Zhang, L. A. Li, N. Gao, G. J. He and H. D. Li, *Small Methods*, 2024, **8**, 2300746.
14 J. Kim, M. S. Choi, K. H. Shin, M. Kota, Y. B. Kang, S. Lee, J. Y. Lee and H. S. Park, *Adv. Mater.*, 2019, **31**, 1803444.
15 Z. H. Tian, Y. Zhang, J. X. Zhu, Q. Y. Li, T. X. Liu and M. Antonietti, *Adv. Energy Mater.*, 2021, **11**, 2102489.
16 Y. X. Chen, B. J. Xi, M. Huang, L. L. Shi, S. Z. Huang, N. N. Guo, D. Li, Z. C. Ju and S. L. Xiong, *Adv. Mater.*, 2022, **34**, 2108621.
17 Y. S. Wang, Z. P. Wang, Y. J. Chen, H. Zhang, M. Yousaf, H. S. Wu, M. C. Zou, A. Y. Cao and R. P. S. Han, *Adv. Mater.*, 2018, **30**, 1802074.
18 Z. H. Yan, Q. W. Yang, Q. H. Wang and J. M. Ma, *Chin. Chem. Lett.*, 2020, **31**, 583–588.
19 W. X. Yang, J. H. Zhou, S. Wang, W. Y. Zhang, Z. C. Wang, F. Lv, K. Wang, Q. Sun and S. J. Guo, *Energy Environ. Sci.*, 2019, **12**, 1605–1612.
20 Z. F. Li, C. Bommier, Z. Sen Chong, Z. L. Jian, T. W. Surta, X. F. Wang, Z. Y. Xing, J. C. Neuefeind, W. F. Stickle, M. Dolgos, P. A. Greaney and X. L. Ji, *Adv. Energy Mater.*, 2017, **7**, 1602894.
21 M. H. Zhang, Y. Li, F. Wu, Y. Bai and C. Wu, *Nano Energy*, 2021, **82**, 105738.
22 D. H. Jeon, *Energy Storage Mater.*, 2019, **18**, 139–147.
23 S. F. Lei, X. F. Chen, B. B. Xiao, W. T. Zhang and J. Liu, *ACS Appl. Mater. Interfaces*, 2019, **11**, 28830–28840.
24 M. Chen, W. Wang, X. Liang, S. Gong, J. Liu, Q. Wang, S. J. Guo and H. Yang, *Adv. Energy Mater.*, 2018, **8**, 1800171.
25 W. D. Qiu, H. B. Xiao, Y. Li, X. H. Lu and Y. X. Tong, *Small*, 2019, **15**, 1901285.
26 C. Lu, Z. T. Sun, L. H. Yu, X. Y. Lian, Y. Y. Yi, J. Li, Z. F. Liu, S. X. Dou and J. Y. Sun, *Adv. Energy Mater.*, 2020, **10**, 2001161.
27 R. L. Huang, X. X. Zhang, Z. X. Qu, X. D. Zhang, J. Lin, F. Wu, R. J. Chen and L. Li, *J. Mater. Chem. A*, 2022, **10**, 682–689.
28 W. Wang, L. Shang, G. J. Chang, C. Y. Yan, R. Shi, Y. X. Zhao, G. I. N. Waterhouse, D. J. Yang and T. R. Zhang, *Adv. Mater.*, 2019, **31**, 1808276.
29 T. Sun, W. J. Zang, H. Yan, J. Li, Z. Q. Zhang, Y. F. Bu, W. Chen, J. Wang, J. Lu and C. L. Su, *ACS Catal.*, 2021, **11**, 4498–4509.
30 J. M. Chen, Y. Cheng, Q. B. Zhang, C. Luo, H. Y. Li, Y. Wu, H. H. Zhang, X. Wang, H. D. Liu, X. He, J. J. Han, D. L. Peng, M. L. Liu and M. S. Wang, *Adv. Funct. Mater.*, 2021, **31**, 2007158.
31 J. H. Han, I. Johnson, Z. Lu, A. Kudo and M. W. Chen, *Nano Lett.*, 2021, **21**, 6504–6510.
32 V. Augustyn, P. Simon and B. Dunn, *Energy Environ. Sci.*, 2014, **7**, 1597–1614.
33 C. Cui, Z. X. Wei, G. Zhou, W. F. Wei, J. M. Ma, L. B. Chen and C. C. Li, *J. Mater. Chem. A*, 2018, **6**, 7088–7098.
34 P. Ge, H. S. Hou, S. J. Li, L. P. Huang and X. B. Ji, *ACS Appl. Mater. Interfaces*, 2018, **10**, 14716–14726.
35 Z. H. Gan, J. Y. Yin, X. Xu, Y. H. Cheng and T. Yu, *ACS Nano*, 2022, **16**, 5131–5152.
36 B. Zhao, Q. Q. Liu, Y. J. Chen, Q. Liu, Q. Yu and H. B. Wu, *Adv. Funct. Mater.*, 2020, **30**, 2002019.

37 P. Song, S. Q. Wei, J. Di, J. Du, W. J. Xu, D. B. Liu, C. D. Wang, S. C. Qiao, Y. Y. Cao, Q. L. Cui, P. J. Zhang, L. B. Ma, J. W. Cui, Y. Wang and Y. J. Xiong, *Nano Res.*, 2023, **16**, 4874–4879.
38 Y. M. Li, Y. S. Hu, M. M. Titirici, L. Q. Chen and X. J. Huang, *Adv. Energy Mater.*, 2016, **6**, 1600659.
39 F. J. Kong, Z. S. Han, S. Tao and B. Qian, *J. Energy Chem.*, 2021, **55**, 256–264.
40 H. L. Deng, L. Wang, S. Y. Li, M. Zhang, T. Wang, J. Zhou, M. X. Chen, S. Chen, J. H. Cao, Q. S. Zhang, J. Zhu and B. A. Lu, *Adv. Funct. Mater.*, 2021, **31**, 2107246.
41 Z. X. Pei, Q. Q. Meng, L. Wei, J. Fan, Y. Chen and C. Y. Zhi, *Energy Storage Mater.*, 2020, **28**, 55–63.
42 P. Wei, Y. Cheng, X. L. Yan, W. B. Ye, X. N. Lan, L. A. Wang, J. J. Sun, Z. Y. Yu, G. F. Luo, Y. Yang, M. H. Rummeli and M. S. Wang, *Adv. Mater.*, 2021, **33**, 2105228.